ACS APPLIED ELECTRONIC MATERIALS

pubs.acs.org/acsaelm

Article

Engineering the Microstructure and Functional Properties of $0.5Ba(Zr_{0.2}Ti_{0.8})O_3$-$0.5(Ba_{0.7}Ca_{0.3})TiO_3$ Thin Films

Sabi W. Konsago, Katarina Žiberna, Aleksander Matavž, Barnik Mandal, Sebastjan Glinšek, Yves Fleming, Andreja Benčan, Geoff L. Brennecka, Hana Uršič, and Barbara Malič*

Cite This: ACS Appl. Electron. Mater. 2024, 6, 4467−4477

Read Online

ACCESS | Metrics & More | Article Recommendations | Supporting Information

ABSTRACT: Lead-free piezoelectric $0.5Ba(Zr_{0.2}Ti_{0.8})O_3$-$0.5(Ba_{0.7}Ca_{0.3})TiO_3$ (BZT−BCT) thin films deposited by chemical solution deposition on platinized silicon substrates using ethylene glycol and ethanol solvents for alkaline-earth carboxylates and transition-metal alkoxides, respectively, are studied. Undoped and manganese-doped BZT-BCT films prepared by repeated deposition of a 0.1 M precursor solution and multistep annealing at 850 °C until reaching the thickness of about 120 nm exhibit a predominantly columnar microstructure with preferential (111) orientation of the perovskite phase. The Mn-doped films' room-temperature permittivity is about 670 at 1 kHz, which is ≈30% higher than the permittivity of their undoped counterparts at the same frequency and temperature while maintaining a similar tan $\delta \approx 0.02$. Mn-doping effectively reduces the leakage of BZT-BCT films, contributing to a saturated ferroelectric hysteresis loop with a remnant polarization of 5 μC cm^{-2} and a coercive field of 80 kV cm^{-1}. The maximum polarization and recoverable energy storage density are about 32 μC cm^{-2} and 10 J cm^{-3}, respectively, with 69% efficiency at 1160 kV cm^{-1}. The energy-storage properties remain almost unaffected after 2 million cycles at a field of 800 kV cm^{-1}. The piezoelectric d_{33} coefficient measured by double-beam laser interferometry is about 20 pm V^{-1}, while the corrected value of $d_{33} \approx 34$ pm V^{-1} taking into account the ratio of the electrode size to substrate thickness being equal to unity.

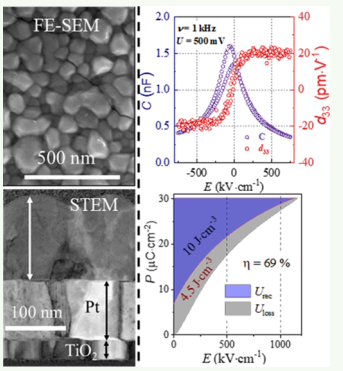

KEYWORDS: *$Ba(Zr_{0.2}Ti_{0.8})O_3$-$(Ba_{0.7}Ca_{0.3})TiO_3$ thin films, chemical solution deposition, crystallinity, dielectric permittivity, ferroelectric, piezoelectric response, energy storage*

1. INTRODUCTION

In the last two decades, legislation to restrict the use of certain hazardous substances, including lead (Pb), in electrical and electronic equipment by some countries, including the European Union, Japan, and the United States,[1−3] has triggered intensive research on lead-free piezoelectric ceramic materials that could be an alternative to lead zirconate titanate ($Pb(Zr_xTi_{1-x})O_3$, PZT), which is known for its excellent piezoelectric properties.[4] Barium zirconate titanate-barium calcium titanate ($0.5(Ba(Zr_{0.2}Ti_{0.8})O_3$-$0.5(Ba_{0.7}Ca_{0.3})TiO_3$, BZT-BCT) is among the promising lead-free ferroelectric materials with a piezoelectric response comparable to that of PZT ceramic.[5,6] Its large piezoelectric response was attributed to the morphotropic phase boundary (MPB) separating rhombohedral $Ba(Zr_{0.2}Ti_{0.8})O_3$ and tetragonal $(Ba_{0.7}Ca_{0.3})TiO_3$ by Liu and Ren in 2009.[5] Later, Keeble et al. reported the existence of a bridging orthorhombic phase between the rhombohedral and tetragonal phases.[7] Acosta et al. pointed out that the high-signal piezoelectric coefficients were related to the transition from tetragonal to orthorhombic phases.[8]

The large piezoelectric d_{33} coefficient in BZT−BCT bulk ceramic with the Curie temperature (T_c) of about 85 °C (the value depends on the grain size)[9] shows the potential of this material for versatile applications. A prototype intravascular ultrasound transducer was designed using BZT-BCT ceramics and tested by X. Yan et al. in 2013.[10] Biocompatibility and good piezoelectric properties make BZT-BCT attractive for biomedical applications.[11] BZT-BCT is becoming an interesting material for energy storage applications. The performance of energy storage capacitors is evaluated by energy storage density and energy storage efficiency, which are related to high saturated polarization, low remanent polarization, and low energy loss density.[12] A few articles reported good energy storage properties of bulk ceramic and thin films of Ca- and Zr-modified barium titanate (BT).[13−15]

BZT-BCT thin films are a viable option in terms of device miniaturization. In chemical solution deposition (CSD) of BZT-BCT thin films, the majority of studies followed the carboxylic acid-based route originally applied for BT,[16,17] with a carboxylic (acetic) acid and alcohol serving as solvents for alkaline-earth carboxylates and transition-metal alkoxides, respectively. How-

Received: March 26, 2024
Revised: May 7, 2024
Accepted: May 9, 2024
Published: May 17, 2024

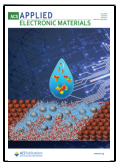

https://doi.org/10.1021/acsaelm.4c00530
ACS Appl. Electron. Mater. 2024, 6, 4467−4477

ever, BZT-BCT thin films by acetic-acid-based CSD often exhibited porosity, fine equiaxed grains, cracks, and, in some cases, chemical inhomogeneity.[18−21] BZT-BCT films prepared by single, double-, or multistep annealing at temperatures of 750−950 °C consisted of equiaxed grains.[20,22−26] Changes in the solution chemistry, such as introducing complexing agents, bi- or multifunctional solvents, or modifiers, were reported to increase the stability of the coating solutions.[19,21] On the other hand, increasing the organic content in the precursor may contribute to carbonaceous residues in the heterometallic framework requiring high decomposition temperatures, thus increasing the porosity in the films.[27]

A possible solution for obtaining a predominantly columnar microstructure in BZT-BCT films that presumably contributes to enhanced functional properties would be depositing a strongly diluted coating solution combined with multistep annealing as shown for BT thin films.[28] Following a similar procedure, a columnar microstructure was obtained in (Ba,Sr)-TiO_3 films.[29−31] In $Ba(Zr,Ti)O_3$ thin films, the grain size decreases with an increasing Zr content of 20% or more, with a concomitant decrease of dielectric permittivity. The films were prepared by a single annealing step at temperatures ranging from 900 to 1200 °C.[32−34] A similar trend of decreasing permittivity with increasing Ca-fraction was observed in $(Ba,Ca)TiO_3$ films.[35,36]

In our preliminary studies on CSD of BZT-BCT films using the acetic-acid-based route with alkaline-earth acetates and transition-metal butoxides diluted with 2-methoxyethanol, the precipitation of the coating solutions was observed after a few days. This was presumably due to the uncontrolled hydrolysis of the alkoxides by the in situ produced water in the esterification reaction of the two solvents. We investigated BT as a reference material for BZT-BCT thin films.[37] A bifunctional alcohol, ethylene glycol ($OHCH_2CH_2OH$, EG), was selected as the solvent for barium acetate, thereby eliminating the possibility of uncontrolled hydrolysis. The stability of the solution was extended from weeks to more than one year. Furthermore, introducing ethanol (EtOH) as the solvent for Ti-butoxide instead of 2-methoxyethanol downshifted the temperature range of organic residue decomposition for a few 100 °C. EG has previously been used in CSD of BZT-BCT films as a modifier[19] but not as the solvent for alkaline-earth reagents. Livage et al. used EG as the solvent for lead acetate in CSD of $Pb(Zr,Ti)O_3$ films.[38] (Note that both EG and EtOH quickly pick up water from the atmosphere if they are not kept dry.)

In this study, BZT-BCT thin films are deposited from the EG-EtOH-based coating solution. Upon multistep annealing at 850 °C, a predominantly columnar microstructure develops. With manganese doping, the leakage current is reduced. The dielectric, ferroelectric, energy-storage, and piezoelectric properties of the manganese-doped BZT-BCT films are reported.

2. EXPERIMENTAL METHODS

For the preparation of $0.5(Ba(Zr_{0.2}Ti_{0.8})O_3\text{-}0.5(Ba_{0.7}Ca_{0.3})TiO_3$, BZT−BCT thin films, alkaline-earth acetates barium acetate ($Ba(CH_3COO)_2$, $Ba(OAc)_2$) with a purity of 99.97%, Sigma-Aldrich, St. Louis, Missouri, USA, and calcium acetates ($Ca(CH_3COO)_2$, $Ca(OAc)_2$) 99.999%, Alfa Aesar, Karlsruhe, Germany, and transition-metal alkoxides: titanium butoxide ($Ti(OC_4H_9)_4$, $Ti(OnBu)_4$) 99.61% and zirconium butoxide ($Zr(OC_4H_9)_4$, $Zr(OnBu)_4$), 80% both purchased from Alfa Aesar, Karlsruhe, Germany, are used as reagents. The molar ratio of barium, calcium, zirconium, and titanium reagents is 0.85:0.15:0.1:0.9. Ethylene glycol ($OHCH_2CH_2OH$, EG, 99.8%) and absolute ethanol (CH_3CH_2OH, EtOH 99.9%) both from Sigma-Aldrich, St. Louis, Missouri, USA, were used to dissolve alkaline-earth acetates and to dilute transition-metal alkoxides, respectively. The volume ratio of EG/EtOH was kept at 3/2. The reagents and solvents were kept and manipulated in an inert atmosphere (N_2-filled glovebox). The solutions of alkaline-earth acetates and transition-metal alkoxides were mixed at room temperature, with the concentration adjusted to either 0.2 or 0.1 M as described in Figure 1. Manganese acetate

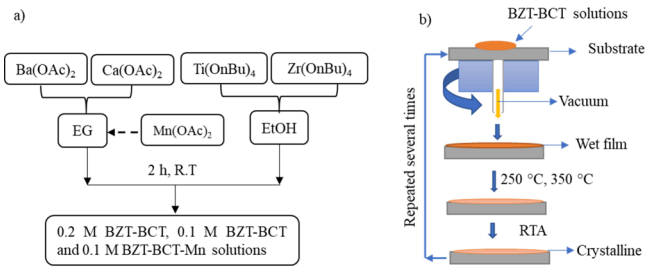

Figure 1. (a) Schematic preparation of BZT-BCT and BZT-BCT-Mn coating solutions. (b) BZT-BCT thin-film deposition. RTA: rapid thermal annealing.

($Mn(CH_3COO)_2$, $Mn(OAc)_2$) 98%, Alfa Aesar, Karlsruhe, Germany, in the amount of 1 mol % was included in the solution of alkaline-earth acetates before mixing with the solution of transition-metal alkoxides. The Mn dopant was added over stoichiometrically. The solution with a 0.1 M concentration, further denoted as 0.1 M BZT-BCT-Mn, was prepared following the same procedure as described above.

The 0.2 M BZT-BCT coating solution was deposited on a 625 μm thick $Pt(111)/TiO_2/SiO_2/(100)/Si$ substrate (Pt/Si, purchased from SINTEF, Oslo, Norway) by spin coating (WS-400B-6NPP/LITE, Laurell, North Wales, PA, USA) at 3000 rpm for 30 s, followed by drying, pyrolysis, and annealing steps. All steps were repeated four times. The drying and pyrolysis steps were at 250 °C for 15 min and 350 °C for 15 min, respectively, on the hot plate. The annealing temperatures were 800 °C, 850 °C, and 900 °C with a heating rate of 13.3 °C/second for all films, while the times were 15 min for the first and the last deposited layer and 5 min for the intermediate ones in a rapid thermal annealing furnace (Mila 5000, Ulvac-Riko, Yokohama, Japan).

The 0.1 M BZT-BCT and BZT-BCT-Mn-0.1 M solutions were deposited on Pt/Si following the same procedure as described above; only the number of the deposition-heat-treatment steps increased to 10 to reach similar film thicknesses as for the 0.2 M solutions.

In further text, the films prepared from the 0.2 M BZT-BCT, 0.1 M BZT-BCT, and 0.1 M BZT-BCT-Mn solutions are denoted BZT-BCT-0.2 M, BZT-BCT-0.1 M, and BZT-BCT-Mn-0.1 M. The list of the samples and their processing parameters are summarized in Table 1.

The phase composition of the films was characterized by XRD with Cu Kα radiation performed in the 2 theta ranges of 10−39 deg and 40−65 deg to avoid recording the Pt (111) peak on a high-resolution diffractometer (X'Pert PRO, PANalytical, Almelo, The Netherlands) with the following parameters: 128 channel detector X'Celerator with a capture angle of 2.122°, step = 0.034°, time per step = 100 s, soller slit = 0.02 rad, mask 10 mm, divergence and antiscatter slit: 10 mm. The phase analysis is performed using X'Pert High Score Plus software.

A Bruker D8 Discover instrument with Cu Kα radiation (λ = 0.154 nm) was used for grazing incidence X-ray diffraction (GIXRD). The experiment was conducted with an incident angle of 0.5°, scanning the 2θ-range from 20° to 60° with a step of 0.02, and a time per step set of 4 s. The same tool was used for the Ψ-scan ($\theta-2\theta$ scan with different tilt angles, Ψ) with a 1 mm collimator. The measurement was performed in a 2θ- and Ψ-range from 38.5° to 39.3° and from 0° to 10°, respectively. The 2θ-step was 0.02, and the time per step was 90 s.

The plan-view and cross-sectional microstructure of the films were imaged using a Verios 4G HP field emission scanning electron microscope (Thermo Fischer, Waltham, Massachusetts, USA) with an accelerating voltage of 10 kV. A 5 nm thick carbon was precoated using a Precise Etching and Coating System 628A (Gatan, Pleasanton,

https://doi.org/10.1021/acsaelm.4c00530
ACS Appl. Electron. Mater. 2024, 6, 4467−4477

Table 1. List of the Samples and Their Processing Parameters

film	molar concentration	number of depositions	annealing temperature, °C
BZT-BCT-0.2M	0.2	4	800
BZT-BCT-0.2M	0.2	4	850
BZT-BCT-0.2M	0.2	4	900
BZT-BCT-0.1M	0.1	10	850
BZT-BCT-Mn-0.1M	0.1	10	850

California, USA). The average lateral grain size of the BZT-BCT-0.1 M and BZT-BCT-Mn-0.1 M films was determined on the obtained SEM images sing the linear intercept method. At least 300 grains were measured on each sample.

For scanning transmission electron microscopy (STEM) analysis, the BZT-BCT-Mn-0.1 M thin film was prepared into lamella form using a Ga^+-source focused ion beam (FIB) Helios Nanolab 650 HP (Thermo Fischer Scientific, Waltham, MA, USA). The structural STEM analysis was performed with a Cs-corrected ARM200CF (Jeol, Tokyo, Japan), operating at 200 kV. The 4D-STEM data set was acquired with the Merlin pixelated detector (Quantum Detectors, Oxford, U.K.).

The gold top electrodes with a diameter of 200 μm were deposited on the films through a shadow mask by magnetron sputtering (5 Pascal). The contact to the bottom platinum electrode was made by etching a part of the film with a mixture of HF 40%, Alfa Aeser, HCl 37−38%, J.T. Baker, and H_2O in a volume ratio (2:5:20).

The topography, roughness, and local ferroelectric/piezoelectric properties were investigated using tapping atomic force microscopy (AFM) mode and piezo-response force microscopy (PFM) mode on Jupiter XR AFM (AFM, Asylum Research, Santa Barbara, California, USA). The noncoated silicon tips (AC200TS, Oxford Instruments, USA) with a radius of 7 nm were used for scanning in tapping (AC Air Topography, Jupiter XR, Asylum Research, Santa Barbara, California, USA) mode. The root-mean-square roughnesses (rms) were determined in the 3 × 3 μm range. The PFM analyses were performed using a Pt-coated Si tip with a diameter of about 15 nm (OMCL-AC240TM, Olympus, Japan). For PFM scanning, an electrical voltage with an amplitude of 3 V and frequency of 300 kHz was applied between the bottom electrode of the sample and the conductive tip in dual alternating-current resonance tracking (DART) mode. The local hysteresis loops were also measured by PFM as described in[39] using DART switching spectroscopy mode at MFP-3D AFM (Asylum Research, Santa Barbara, California, USA). The sequence of increasing steps of the DC electric field was driven at 20 Hz, and a maximum amplitude of 18 V was applied. The frequency of the triangular envelope was 0.99 Hz. A superimposed sinusoidal AC signal with an amplitude of 3 V and a frequency of ∼350 kHz was used. Three cycles were measured in off-electric field mode.

An impedance analyzer (HP 4284A, Keysight, Santa Rosa, USA) was used to measure the frequency dependence of the dielectric permittivity and losses at room temperature across a frequency range from 100 Hz to 1 MHz, and the dielectric permittivity and losses at temperatures range of 25 to 150 °C from 33 Hz to 100 kHz. The Aixacct TF Analyzer 2000 (Aixacct Systems GmbH, Aachen, Germany) was used to measure the ferroelectric polarization (P), current density (j), and strain (S) hysteresis loops with a sinusoidal test signal at room temperature. In addition, the energy storage properties, namely, energy storage density (U_{st}), recovered energy storage density (U_{rec}), energy loss (U_{loss}), and efficiency (η), were calculated from the unipolar electric field loop with a magnitude of 1160 kV cm^{-1} and a frequency of 1 kHz. Furthermore, the thin-film sample was cycled 2 million times at room temperature with an electric field amplitude of 800 kV cm^{-1}. The two consecutive unipolar hysteresis loops were measured at 1 kHz to monitor the energy storage properties. The data of the unipolar loop of the first E-cycle can be found in the main part of the paper, and the data of the second E-cycle can be found in the Supporting Information. The capacitance as a function of the DC field (C−E_{DC}) was measured at 1 kHz with a small-signal amplitude of 50 mV. The piezoelectric d_{33} coefficient was measured at 1 kHz with a small-signal amplitude of 500 mV with a double-beam laser interferometer (DBLI, Aixacct Systems GmbH, Aachen, Germany).

3. RESULTS AND DISCUSSION

3.1. Phase Composition and Microstructure of BZT-BCT-0.2 M Films. XRD patterns of the BZT-BCT-0.2 M films annealed at 800, 850, and 900 °C are shown in Figure 2. All films

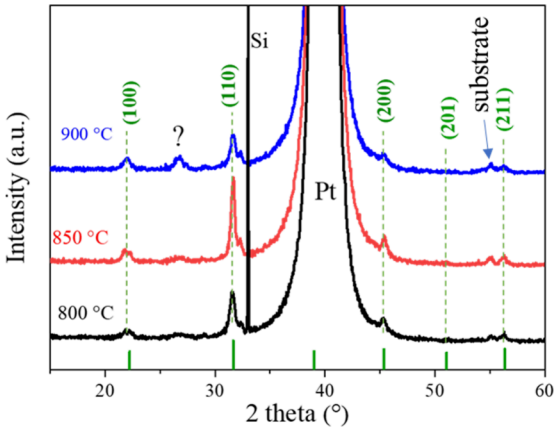

Figure 2. XRD patterns of BZT-BCT-0.2 M films on Pt/Si annealed at different temperatures. The peaks corresponding to the perovskite phase are indexed according to the cubic $BaTiO_3$ phase (PDF 01-074-4539). The question mark indicates an unidentified peak.

crystallized in the perovskite phase. The (110) peak has the highest intensity; however, the Pt (111) peak overlaps with BZT-BCT (111); consequently, the orientation cannot be inferred. We note a low-intensity peak at 2 theta 26.6° in the film annealed at 900 °C, which could indicate a possible reaction of the film with the substrate.

The field emission scanning electron microscopy (FE-SEM) cross-section, plan view, and AFM topography height images of the BZT-BCT-0.2 M thin films are presented in Figure 3. The thickness of the films annealed at 850 and 900 °C is about 120 nm, while the film annealed at 800 °C is about 10 nm thicker due to porosity. In contrast to BT thin films, which at similar deposition and annealing conditions crystallize in columnar microstructure,[37] the BZT-BCT-0.2 M films annealed at 800 and 850 °C have fine equiaxed grains. Studies of BT precursors revealed that the thermal decomposition was concluded at about 800 °C.[40] In comparison, carbonaceous residues were detected in a BZT-BCT precursor up to about 1000 °C.[41]

The surface microstructures reveal that the grain size of the films slightly increases with increasing annealing temperature, reaching about 50 nm at 900 °C, while the porosity decreases. AFM topography height images support FE-SEM analysis. The root-mean-square (rms) roughness of the films annealed at 800 and 850 °C is between 4 and 5 nm notwithstanding the annealing temperature.

https://doi.org/10.1021/acsaelm.4c00530
ACS Appl. Electron. Mater. 2024, 6, 4467−4477

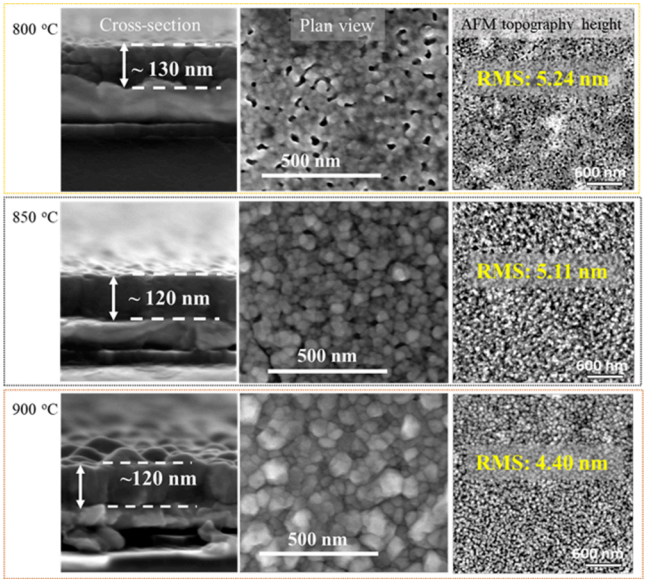

Figure 3. Cross-section (left) and plan-view (middle) FE-SEM micrographs and AFM topography images (right) of BZT-BCT-0.2 M films annealed at 800, 850, and 900 °C.

The dielectric permittivity and losses of the film annealed at 850 °C are about 350 and 0.02 at 1 kHz, respectively, while the films annealed at 800 and 900 °C exhibit lower permittivity of about 260 and 250, respectively, with similar losses at lower frequencies (Table 2). The lower relative permittivity of the film annealed at 800 °C compared to the film annealed at 850 °C could be explained by lower crystallinity and high porosity, while the lower relative permittivity of the film annealed at 900 °C is most likely due to interaction between the film and the substrate supported by a nonidentified low-intensity peak in the XRD pattern, cf. Figure 2. The dielectric data of the films as a function of the frequency are collected in Supporting Information S1. The polarization-electric field (*P-E*) loops show no saturation (see Supporting Information S2) in agreement with the literature on BZT-BCT films prepared following a similar procedure,[21] which could be related to fine grain size and/or leakage. We conclude that 850 °C is the optimal annealing temperature for BZT-BCT thin films with a dense, smooth microstructure without obvious impurities.

Table 2. Dielectric Permittivity and Losses Measured at Room Temperature and at 1 kHz of BZT-BCT-0.2M, BZT-BCT-0.1M, and BZT-BCT-Mn-01M Films Compared with Literature Data[a]

film	conc. of solution	annealing temperature	thickness	ε'	tan δ	ref
BZT-BCT	0.35 M	700 °C	300 nm	220	0.63	55
BZT-BCT	0.2 M	700 °C	400 nm	377	0.22	56
BZT-BCT	0.35 M	750 °C	200 nm	280	0.04	20
BZT-BCT	0.35 M	700 °C	450 nm	157	0.03	57
BZT-BCT-0.2M	0.2 M	800 °C	130 nm	260	0.02	this work
BZT-BCT-0.2M	0.2 M	850 °C	120 nm	350	0.02	this work
BZT-BCT-0.2M	0.2 M	900 °C	120 nm	250	0.02	this work
BZT-BCT-0.1M	0.1 M	850 °C	120 nm	~510	0.02	this work
BZT-BCT-Mn-0.1M	0.1 M	850 °C	120 nm	~670	0.02	this work

[a]All films were deposited on Pt/Si substrates.

3.2. Optimization of the Microstructure of the Films.

Lowering the concentration of the coating solution and sequential crystallization of individual layers by multistep annealing enabled the formation of a predominantly columnar microstructure of BT and $SrTiO_3$ thin films.[42] Following such an approach, we diluted the coating solutions to a 0.1 M concentration. Also, we increased the number of deposited layers from 4 to 10 to reach thicknesses similar to those in the case of films deposited from the 0.2 M solution. Furthermore, we introduced Mn-dopant (1 mol %) to reduce the leakage current.[43] The BZT-BCT-0.1 M and BZT-BCT-Mn-0.1 M films on Pt/Si substrates annealed at 850 °C crystallize in the perovskite phase, with the (110) peak being the most intense in both cases (XRD patterns recorded in Bragg−Brentano geometry are collected in Supporting Information S3).

Further XRD analysis was performed to obtain deeper insight into the crystalline orientation of the perovskite phase. GIXRD was measured to enhance the signal coming from the film (Figure 4a). The (111) peak is now nicely revealed, as the Pt signal present in Figure 2 is strongly suppressed. However, GIXRD is not a very convenient method to quantify the orientation of the films, as the scattering vector changes during the 2θ scan and is not normal to the surface of the film.[44,45] Therefore, tilt-angle (Ψ)-dependent XRD patterns were measured around the (111) peak. This enables gradual probing of the peak, going from completely out-of-plane ($\Psi = 0°$) to completely in-plane ($\Psi = 90°$) conditions. The decrease of the peak intensity at $\Psi > 0°$, observed in Figure 4b, therefore indicates a strong (111) out-of-plane orientation of the film. The orientation was further confirmed with a (110) pole figure measurement (see Supporting Information S4).

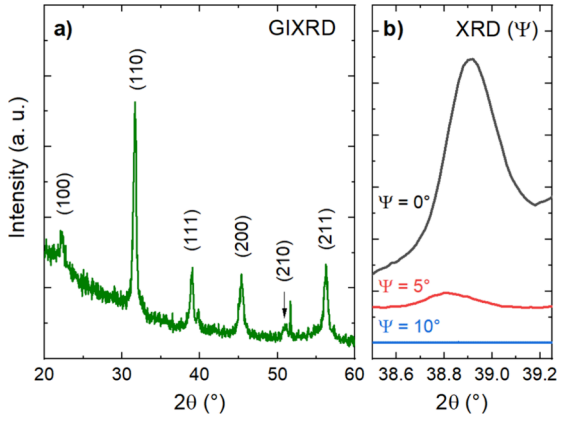

Figure 4. BZT-BCT-Mn-0.1 M film on Pt/Si annealed at 850 °C. (a) GIXRD pattern. Peaks that are not denoted with Miller indices correspond to the substrate. (b) XRD pattern around the (111) peak as a function of a tilt angle (Ψ).

Figure 5 shows plan-view and cross-sectional FE-SEM micrographs of BZT-BCT-0.1 M and BZT-BCT-Mn-0.1 M films. There is no obvious difference in their microstructural features. The surface microstructures are dense and uniform, with average lateral grain sizes of 72 and 74 nm for BZT-BCT-0.1 M and BZT-BCT-Mn-0.1 M, respectively. Their respective thicknesses are about 110 and 120 nm.

https://doi.org/10.1021/acsaelm.4c00530
ACS Appl. Electron. Mater. 2024, 6, 4467−4477

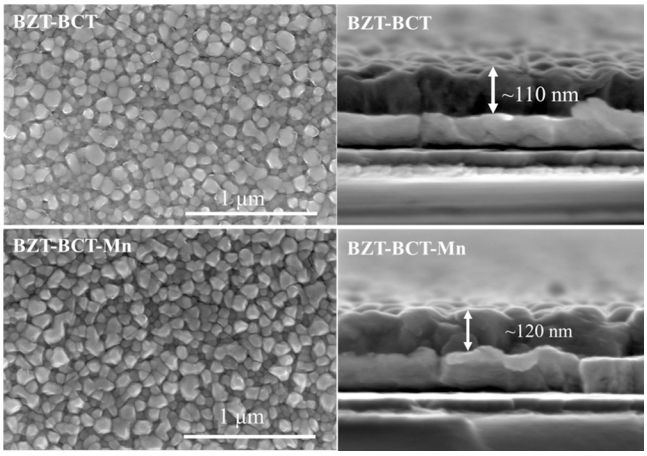

Figure 5. Plan-view (left) and cross-section (right) FE-SEM micrographs of BZT-BCT-0.1 M and BZT-BCT-Mn-0.1 M films on Pt/Si, annealed at 850 °C.

We noticed the appearance of cracks in thicker films, which we attributed to a large thermal expansion mismatch between the film and the silicon substrate. BZT-BCT ceramic and silicon thermal expansion coefficients are $\approx 12 \times 10^{-6}$/K between 100 and 600 °C[46] and $\approx 3 \times 10^{-6}$/K,[47] respectively.

Figure 6a shows the STEM micrographs of the cross-section of the BZT-BCT-Mn-0.1 M film at different magnification scales. The microstructure consists of predominantly columnar grains extending throughout the thickness of the film, as well as some fine equiaxed grains. The bright-field STEM images of a single columnar grain (center and far-right parts of panel a) reveal boundaries between about 10 nm thick individual layers that formed upon repeating the deposition/annealing steps. Each newly deposited layers crystallize on top of preceding layers, and such homoepitaxial growth within individual columnar grains was previously observed in CSD-derived barium and strontium titanate thin films.[48]

The selected area electron diffraction (SAED) pattern is shown in Figure 6b. We note that the grains in the film are preferentially [111] and to a minor degree [110] oriented, according to SAED, in agreement with GIXRD analysis; see Figure 4. The platinum substrate is [111] oriented and has a small lattice mismatch with the BZT-BCT film, so it may serve as a nucleation layer for [111] oriented BZT-BCT columnar grains. Jia and Urban found a [111] orientational relationship between the Pt substrate and columnar grains in the $SrTiO_3$ film. Interestingly, the microstructure of $BaTiO_3$ film on Pt substrate was columnar but without texture, which was attributed to a different mechanism of phase formation involving Ba-Ti-oxycarbonate.[48]

Figure 6c shows the center of mass (CoM) vector magnitude image.[49] Different contrast observed within individual grains infers the existence of domain walls, as indicated by the arrows in the CoM vector magnitude image. We may conclude that columnar grains are multidomain.

Figure 7 shows the chemical analysis of the BZT-BCT-Mn-0.1 M film obtained by energy-dispersive X-ray spectroscopy (EDS) mapping (STEM-EDS). The clear interface between the film and the substrate evidence that the film does not react with the substrate upon annealing at 850 °C. The EDS analysis reveals a homogeneous distribution of elements across the film thickness. This indicates that the crystallization from the amorphous phase occurs without segregation, i.e., the chemical homogeneity of the amorphous phase is retained during the crystallization of the perovskite phase. We note that manganese could not be detected due to its low concentration, which implies that it is not segregated but rather homogeneously distributed in the perovskite matrix.

3.3. Functional Properties of BZT-BCT-0.1 M and BZT-BCT-Mn-0.1 M Films. Figure 8 shows the dielectric permittivity and losses of BZT-BCT-0.1 M and BZT-BCT-

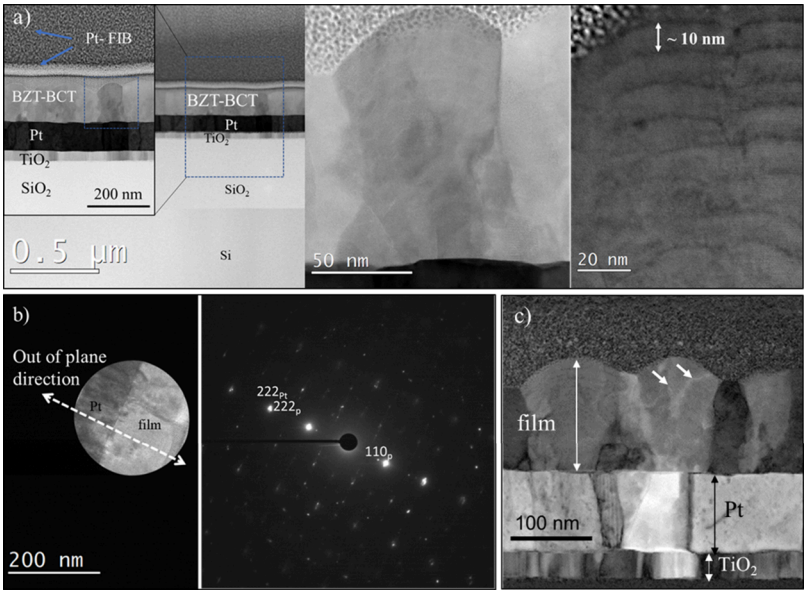

Figure 6. (a) Bright-field STEM images of a cross-section of BZT-BCT-Mn-0.1 M film on Pt/Si at different magnifications. (b) SAED pattern (right) of the selected region (left). Both the (110) and (111) planes of BZT-BCT-Mn, which are perpendicular to the film substrate, are parallel to the (111) Pt planes. The direction perpendicular to the film substrate is indicated by a double arrow on the image of the selected region, which was taken across ~4 perovskite (p) and ~5 Pt grains. (c) Magnitude map of the vector field calculated from the center of mass (CoM) image showing the existence of different domains in the grains.

https://doi.org/10.1021/acsaelm.4c00530
ACS Appl. Electron. Mater. 2024, 6, 4467−4477

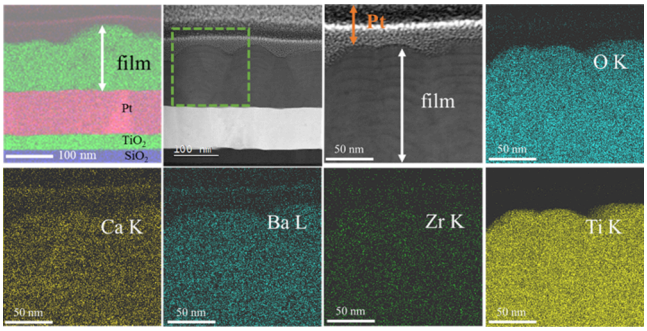

Figure 7. EDS-STEM compositional analysis of the BZT-BCT-Mn-0.1 M film on a Pt/Si substrate. For the EDS mapping, the spectral lines O K, Ca K, Ba L, Zr K, and Ti K were used. The upper layer of Pt is due to FIB preparation.

Mn-0.1 M films at different frequencies in the 25 to 200 °C temperature range. The room-temperature dielectric permittivity and tan δ losses of the BZT-BCT-0.1 M film at 1 kHz are about 510 and 0.02, respectively. It is difficult to determine the Curie temperature because the permittivity and losses also increase with increasing temperature, which we connect to the increased conductivity of the film. The hardly discernible permittivity peak is estimated to be around 70−90 °C. This temperature range is roughly comparable to the reported Curie temperature in BZT-BCT bulk ceramic.[9,50]

The BZT-BCT-Mn-0.1 M film exhibits dielectric permittivity of about 30% higher than its undoped counterpart while maintaining a similar tan $\delta \approx 0.02$ at room temperature. With increasing temperature, its lossy behavior is effectively reduced due to manganese doping.[51−53] The strongly broadened dielectric permittivity peak is at about 55−75 °C. Lowering the Curie temperature upon manganese doping observed in the studied films was also reported for other perovskite oxides.[52,54] Despite a broad peak due to presumed phase transition, the dielectric properties are almost temperature-independent ($\Delta\varepsilon <$ 5% between 25 °C − 125 °C), which is favorable for implication in many applications.

In Table 2, the room-temperature dielectric properties of our films are compared with literature data.[20,55−57] In our case, the coating solution concentration and the film thickness are lower and the annealing temperature is higher. Still, the dielectric permittivity is about two times higher, and losses are comparable or lower than the literature data. This increase in the permittivity is attributed to the dense columnar microstructure.

Local ferro- and piezoelectric properties of both films BZT-BCT-0.1 M and BZT-BCT-Mn-0.1 M are investigated by the piezo-response force module of AFM (Figure 9). The topography height and deflection AFM images reveal a dense, uniform microstructure consistent with the FE-SEM micrograph shown in Figure 5. The surface roughness is about 4.5 and 4 nm for BZT-BCT-0.1 M and BZT-BCT-Mn-0.1 M films, respectively. The PFM amplitude (c) and phase (d) images show different contrasts under the applied voltage, indicating the local piezoelectric/ferroelectric response in both films, which is also confirmed by the PFM amplitude (e) and phase (f) hysteresis loops.

Figure 10a shows the *P-E* loops of BZT-BCT-0.1 M and BZT-BCT-Mn-0.1 M films. The manganese-doped film has a saturated *P-E* hysteresis loop, with remanent polarization P_r of 5 μC cm^{-2}, coercive field E_c of 80 kV cm^{-1}, and maximum polarization P_s of 32 μC cm^{-2} at an electric field of 1160 kV cm^{-1}. A saturated hysteresis *P-E* loop could not be obtained in the undoped BZT-BCT-0.1 M film that only survived electric fields below 300 kV cm^{-1} without breakdown. To evaluate the

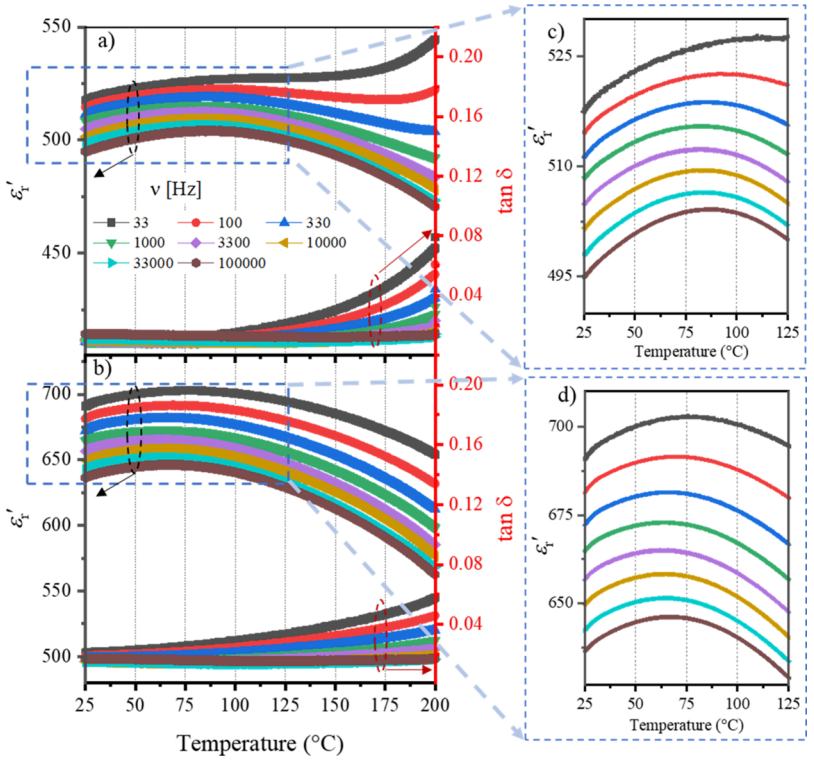

Figure 8. Dielectric permittivity (ε_r') and losses (tan δ) as a function of temperature at different frequencies (ν) of (a) BZT-BCT-0.1 M and (b) BZT-BCT-Mn-01 M films on Pt/Si annealed at 850 °C. (c, d) Magnified *y* scale of ε_r'.

https://doi.org/10.1021/acsaelm.4c00530
ACS Appl. Electron. Mater. 2024, 6, 4467−4477

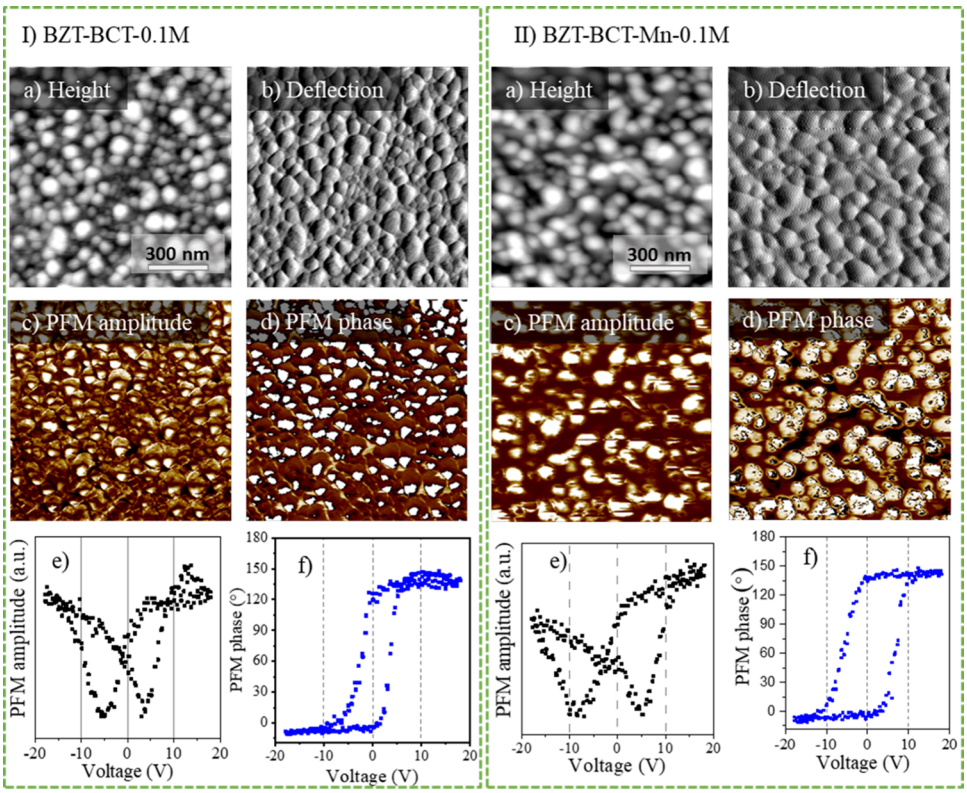

Figure 9. AFM topography (a) height and (b) deflection images, PFM (c) amplitude and (d) phase images, PFM (e) amplitude and (f) phase hysteresis loops of (I) BZT-BCT-0.1 M and (II) BZT-BCT-Mn-0.1 M films on Pt/Si annealed at 850 °C. The second and third cycles are shown in panels (e) and (f).

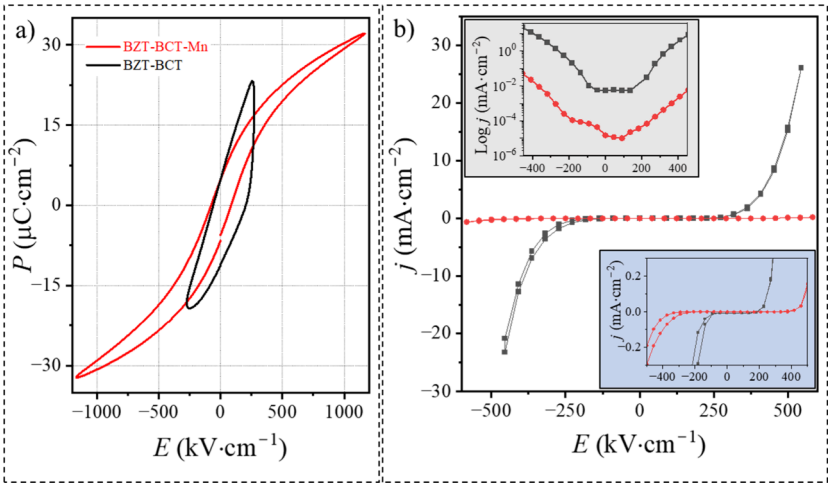

Figure 10. (a) *P-E* loops and (b) *j-E* dependence of BZT-BCT-0.1 M and BZT-BCT-Mn-0.1 M films on Pt/Si. Top inset in panel (b): logarithmic *y*-axis, bottom inset in panel (b): magnified linear *y*-axis. The *P-E* and *j-E* measurements were performed at 1 kHz.

effect of Mn doping on BZT-BCT film, the current density (j) under an applied electric field was measured in both films, see Figure 10b. The leakage current density in the BZT-BCT-0.1 M film is about 15 mA·cm^{-2} at the applied field of 500 kV cm^{-1}. Manganese doping significantly reduces the leakage to about 0.18 mA cm^{-2} in the same field. The effect of Mn-doping on the leakage current at low fields is clearly seen on the logarithmic scale; see the inset of Figure 10b.

Due to the slim *P -E* loop, high maximum polarization, high breakdown field, and low current density, cf. Figure 10, the BZT-BCT-Mn-0.1 M films could be considered for energy storage. Figure 11 shows the unipolar *P-E* loop measured at 1 kHz (first cycle). The calculated energy storage density (U_{st}), recovered energy storage density (U_{rec}), energy loss (U_{loss}), and efficiency (η) are 14.5, 10, 4.5 J cm^{-3}, and 69%, respectively, at 1160 kV cm^{-1}. These properties are comparable to the energy storage properties of the PZT thin film deposited on (001) $SrRuO_3$/$SrTiO_3$/Si by pulsed laser deposition (PLD).[58] The U_{rec} of (Ba,Ca)(Zr,Ti)O_3 films prepared by PLD and ion beam sputtering deposition were reported to be 39 J·cm^{-3} and 2.3 J·cm^{-3}, respectively, with the respective η of 33% and 28.5%.[15,59]

https://doi.org/10.1021/acsaelm.4c00530
ACS Appl. Electron. Mater. 2024, 6, 4467−4477

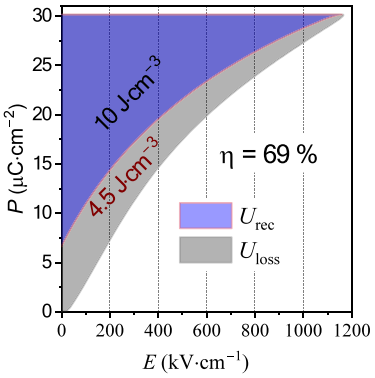

Figure 11. Energy storage properties obtained from the unipolar *P-E* loop (first cycle) of a BZT-BCT-Mn-0.1 M thin film on Pt/Si annealed at 850 °C.

In our case, η is about twice as high as compared to the film prepared by PLD, which has a higher U_{rec}.

Furthermore, the BZT-BCT-Mn-0.1 M film's endurance was measured by electric field cycling two consecutive unipolar *P-E* loops at 800 kV cm^{-1} with a frequency of 1 kHz, see Figure 12.

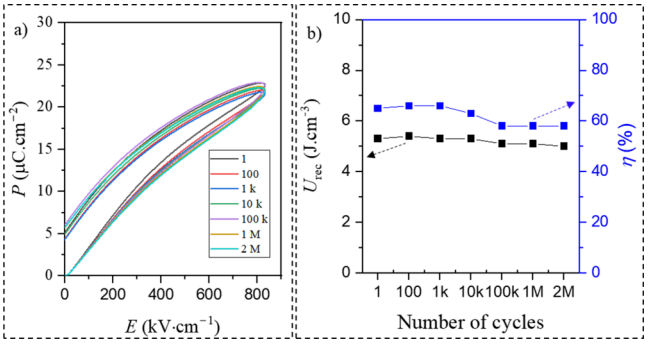

Figure 12. (a) Unipolar P-E loops and (b) U_{rec} and η of BZT-BCT-Mn-0.1 M film upon electric field cycling.

After 2 million cycles, there is no significant change in the *P-E* loops. The U_{rec} of 5.3 J cm^{-3} is linear upon cycling, while the efficiency of about 65% is slightly decreased down to 58% above 10^5 cycles. A similar value and linear behavior of U_{rec} are also observed from the data calculated using the second-cycle *P-E* loops (Supporting Information S5). Here, the energy storage efficiency (η) is slightly higher than the value from the first cycle. This can be explained by the fact that in the second cycle, the sample is already partially poled, reducing the charging energy and increasing the efficiency.

The field-induced strain (*S-E*), capacitance tunability (*C-E*), and the extracted piezoelectric d_{33} coefficient of BZT-BCT-Mn-0.1 M film were obtained by double-beam laser interferometry (DBLI), see Figure 13. The maximum field-induced strain is 0.18% at 1 MV·cm^{-1} measured at 1 kHz. A very similar value was obtained at 100 Hz. The capacitance response to the electric field indicates the switching behavior of domains, thus confirming the ferroelectricity of the film.[19] The calculated and plotted relative permittivity as a function of the electric field (see Figure 13b) matches the value of permittivity obtained by temperature-dependent dielectric measurements. The small-signal d_{33} coefficient of BZT-BCT-Mn-0.1 M measured on an electrode with a diameter of 200 μm is about 22 pm V^{-1}. The value of d_{33} is likely somewhat underestimated due to the small ratio between the electrode size and the substrate thickness (0.32). Ideally, the ratio should be around 1,[60] as also supported by our previous study.[61] The corrected value, considering the respective ratio of 1, is about 34 pm V^{-1}. To our knowledge, macroscopic measurement of the field-induced strain of BZT-BCT films has not been reported previously.

4. CONCLUSIONS AND OUTLOOK

In summary, we investigated the microstructure and functional properties of BZT-BCT thin films deposited on the platinized silicon substrates. The films were undoped or doped with manganese. By carefully designed processing, which included adapted solution chemistry that prevented uncontrolled hydrolysis of transition-metal reagents, diluting the coating solution to decrease the thickness of individual deposited layers, and multistep annealing at 850 °C, BZT-BCT films crystallized with a columnar microstructure. The perovskite phase was preferentially (111) oriented, as shown by GIXRD and supported by STEM analysis. The STEM-EDS analysis revealed a homogeneous distribution of elements across the film thickness, indicating that the homogeneity of the solid solution was retained upon crystallization.

The room-temperature dielectric permittivity of the films with a columnar microstructure was 510, almost twice as much as the value obtained in the film with a fine, granular microstructure, in agreement with the dielectric grain-size effect. Manganese

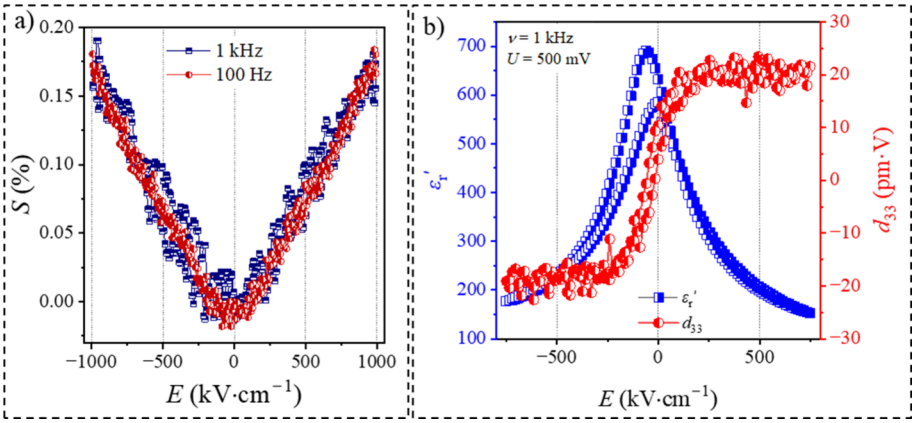

Figure 13. Electric field dependence of (a) strain and (b) dielectric permittivity (ε_r') and small-signal piezoelectric d_{33} coefficient of BZT-BCT-Mn film on Pt/Si prepared from 0.1 M coating solution and annealed at 850 °C measured by DBLI.

https://doi.org/10.1021/acsaelm.4c00530
ACS Appl. Electron. Mater. 2024, 6, 4467−4477

doping contributed to a higher room-temperature dielectric permittivity (670), a downshift of a very broad permittivity peak, and a significant leakage reduction of BZT-BCT thin films. The manganese-doped BZT-BCT films exhibit ferroelectric properties. A slim polarization-electric field loop, high maximum polarization, high breakdown field, and almost fatigue-free response after 2 million cycles at 800 kV cm^{-1} make them good candidates for energy-storage applications. The piezoelectric response of BZT-BCT was confirmed by DBLI.

Future research could focus on the multifunctionality of BZT-BCT thin films following the proposed processing approach and possibly using other substrates, such as platinized sapphire or metal foils, for versatile energy conversion applications.

■ ASSOCIATED CONTENT

Supporting Information

The Supporting Information is available free of charge at https://pubs.acs.org/doi/10.1021/acsaelm.4c00530.

Frequency dependence of dielectric permittivity (ε_r') and losses (tan δ) at room temperature of BZT-BCT-0.2 M annealed at different temperatures; electric-field dependence of the electrical polarization of BZT-BCT-0.2 M films annealed at different temperatures; XRD patterns of BZT-BCT-0.1 M and BZT-BCT-Mn-0.1 M films on Pt/Si annealed at 850 °C recorded in Bragg−Brentano geometry; and unipolar *P-E* loops and recoverable energy density (U_{rec}) and efficiency (η) of BZT-BCT-Mn-0.1 M film upon electric field cycling (PDF)

■ AUTHOR INFORMATION

Corresponding Author

Barbara Malič − *Electronic Ceramics Department, Jožef Stefan Institute, 1000 Ljubljana, Slovenia; Jožef Stefan International Postgraduate School, 1000 Ljubljana, Slovenia;* Email: barbara.malic@ijs.si

Authors

Sabi W. Konsago − *Electronic Ceramics Department, Jožef Stefan Institute, 1000 Ljubljana, Slovenia; Jožef Stefan International Postgraduate School, 1000 Ljubljana, Slovenia;* orcid.org/0000-0002-2880-5543

Katarina Žiberna − *Electronic Ceramics Department, Jožef Stefan Institute, 1000 Ljubljana, Slovenia; Jožef Stefan International Postgraduate School, 1000 Ljubljana, Slovenia*

Aleksander Matavž − *Condensed Matter Physics Department, Jožef Stefan Institute, 1000 Ljubljana, Slovenia*

Barnik Mandal − *Materials Research and Technology Department (MRT), Luxembourg Institute of Science and Technology (LIST), L-4422 Belvaux, Luxembourg; University of Luxembourg, L-4422 Belvaux, Luxembourg*

Sebastjan Glinšek − *Materials Research and Technology Department (MRT), Luxembourg Institute of Science and Technology (LIST), L-4422 Belvaux, Luxembourg;* orcid.org/0000-0002-5614-0825

Yves Fleming − *Materials Research and Technology Department (MRT), Luxembourg Institute of Science and Technology (LIST), L-4422 Belvaux, Luxembourg*

Andreja Benčan − *Electronic Ceramics Department, Jožef Stefan Institute, 1000 Ljubljana, Slovenia; Jožef Stefan International Postgraduate School, 1000 Ljubljana, Slovenia*

Geoff L. Brennecka − *Department of Metallurgical and Materials Engineering, Colorado School of Mines, Golden, Colorado 80401, United States;* orcid.org/0000-0002-4476-7655

Hana Uršič − *Electronic Ceramics Department, Jožef Stefan Institute, 1000 Ljubljana, Slovenia; Jožef Stefan International Postgraduate School, 1000 Ljubljana, Slovenia;* orcid.org/0000-0003-4525-404X

Complete contact information is available at: https://pubs.acs.org/10.1021/acsaelm.4c00530

Notes

The authors declare no competing financial interest.

■ ACKNOWLEDGMENTS

Slovenian Research Agency (core funding P2-0105, J7-4637, P1-0125, S.W.K - young researcher programme and bilateral cooperation BI-US/22-24-039), NANOCENTER for access to FIB, MSCA-PF grant agreement n° 101110882. Ivana Goričan and Matej Šadl are acknowledged for help related to energy storage properties. The authors thank V. Fišinger for assistance in the AFM laboratory. Barnik Mandal and Sebastjan Glinsek acknowledge the Luxembourg National Research Fund (FNR) for financial support through the project INTER/NWO/20/15079143/TRICOLOR. Geoff Brennecka acknowledges financial support by the Fulbright US Scholar Program, which is sponsored by the US Department of State.

■ REFERENCES

(1) EU-Directive 2002/95/EC. Restriction of the Use of Certain Hazardous Substances in Electrical and Electronic Equipment (RoHS). *Official J. Eur. Union* **2003**, *46* (L37), 19. https://eur-lex.europa.eu/LexUriServ/LexUriServ.do?uri=OJ:L:2003:037:0019:0023:en:PDF

(2) JIS c 0950:2005 (E); *The marking for presence of the specific chemical substances for electrical and electronic equipment*; Japanese Standards Association, 2005, https://www.iaeg.com/binaries/content/assets/iaeg/wg9/rohs-regulatory-alert/japan_rohs-regulation_jis-c-0950_english.pdf (accessed 2024−03−11).

(3) Reczek, K.; Benson, L. M.; *A guide to United States electrical and electronic equipment compliance requirements*; NIST Interagency/Internal Report (NISTIR) 8118r2, 2021, DOI: .

(4) Rödel, J.; Webber, K. G.; Dittmer, R.; Jo, W.; Kimura, M.; Damjanovic, D. Transferring lead-free piezoelectric ceramics into application. *Journal of the European Ceramic Society* **2015**, *35* (6), 1659−1681.

(5) Liu, W.; Ren, X. Large piezoelectric effect in Pb-free ceramics. *Physical review letters* **2009**, *103* (25), No. 257602.

(6) Acosta, M.; Novak, N.; Rossetti, G. A., Jr; Rödel, J. Mechanisms of electromechanical response in (1−x)$Ba(Zr_{0.2}Ti_{0.8})O_3$-x$(Ba_{0.7}Ca_{0.3})TiO_3$ ceramics. *Appl. Phys. Lett.* **2015**, *107* (14), 142906.

(7) Keeble, D. S.; Benabdallah, F.; Thomas, P. A.; Maglione, M.; Kreisel, J. Revised structural phase diagram of $(Ba_{0.7}Ca_{0.3}TiO_3)$-$(BaZr_{0.2}Ti_{0.8}O_3)$. *Appl. Phys. Lett.* **2013**, *102* (9), No. 092903.

(8) Acosta, M.; Novak, N.; Jo, W.; Rödel, J. Relationship between electromechanical properties and phase diagram in the $Ba(Zr_{0.2}Ti_{0.8})$-O_3−x$(Ba_{0.7}Ca_{0.3})TiO_3$ lead-free piezoceramic. *Acta Mater.* **2014**, *80*, 48−55.

(9) Hao, J.; Bai, W.; Li, W.; Zhai, J. Correlation between the microstructure and electrical properties in high-performance $(Ba_{0.85}Ca_{0.15})(Zr_{0.1}Ti_{0.9})O_3$ lead-free piezoelectric ceramics. *J. Am. Ceram. Soc.* **2012**, *95* (6), 1998−2006.

(10) Yan, X.; Lam, K. H.; Li, X.; Chen, R.; Ren, W.; Ren, X.; Shung, K. K. Correspondence: Lead-free intravascular ultrasound transducer using BZT-50BCT ceramics. *IEEE Trans. Sonics Ultrason.* **2013**, *60* (6), 1272−1276.

(11) Scarisoreanu, N. D.; Craciun, F.; Ion, V.; Birjega, R.; Bercea, A.; Dinca, V.; Gruionu, G. Lead-free piezoelectric (Ba,Ca)(Zr,Ti)O_3 thin

films for biocompatible and flexible devices. *ACS Appl. Mater. Interfaces* **2017**, *9* (1), 266−278.
(12) Palneedi, H.; Peddigari, M.; Hwang, G. T.; Jeong, D. Y.; Ryu, J. High-performance dielectric ceramic films for energy storage capacitors: progress and outlook. *Adv. Funct. Mater.* **2018**, *28* (42), No. 1803665.
(13) Puli, V. S.; Pradhan, D. K.; Chrisey, D. B.; Tomozawa, M.; Sharma, G. L.; Scott, J. F.; Katiyar, R. S. Structure, dielectric, ferroelectric, and energy density properties of (1−x)BZT−x BCT ceramic capacitors for energy storage applications. *J. Mater. Sci.* **2013**, *48*, 2151−2157.
(14) Syal, R.; Goel, R.; De, A.; Singh, A. K.; Sharma, G.; Thakur, O. P.; Kumar, S. Flattening of free energy profile and enhancement of energy storage efficiency near morphotropic phase boundary in lead-free BZT-xBCT. *J. Alloys Compd.* **2021**, *873*, No. 159824.
(15) Puli, V. S.; Pradhan, D. K.; Adireddy, S.; Martínez, R.; Silwal, P.; Scott, J. F.; Katiyar, R. S. Nanoscale polarisation switching and leakage currents in $(Ba_{0.955}Ca_{0.045})(Zr_{0.17}Ti_{0.83})O_3$ epitaxial thin films. *J. Phys. D: Appl. Phys.* **2015**, *48* (35), No. 355502.
(16) Hasenkox, U.; Hoffmann, S.; Waser, R. Influence of precursor chemistry on the formation of $MTiO_3$ (M= Ba, Sr) ceramic thin films. *J. Sol-Gel Sci. Technol.* **1998**, *12*, 67−79.
(17) Krupanidhi, S. B.; Peng, C. J. Studies on structural and electrical properties of barium strontium titanate thin films developed by metallo-organic decomposition. *Thin Solid Films* **1997**, *305* (1−2), 144−156.
(18) Kang, G.; Yao, K.; Wang, J. $(1-x)Ba(Zr_{0.2}Ti_{0.8})O_3 - x(Ba_{0.7}Ca_{0.3})TiO_3$ Ferroelectric Thin Films Prepared from Chemical Solutions. *J. Am. Ceram. Soc.* **2012**, *95* (3), 986−991.
(19) Wang, Z.; Cai, Z.; Wang, H.; Cheng, Z.; Chen, J.; Guo, X.; Kimura, H. Lead-free 0.5 $Ba(Ti_{0.8}Zr_{0.2})O_3$ - 0.5$(Ba_{0.7}Ca_{0.3})TiO_3$ thin films with enhanced electric properties fabricated from optimized sol-gel systems. *Mater. Chem. Phys.* **2017**, *186*, 528−533.
(20) Li, W. L.; Zhang, T. D.; Xu, D.; Hou, Y. F.; Cao, W. P.; Fei, W. D. $LaNiO_3$ seed layer induced enhancement of piezoelectric properties in (100)-oriented (1−x) BZT−xBCT thin films. *Journal of the European Ceramic Society* **2015**, *35* (7), 2041−2049.
(21) Barbato, P. S.; Casuscelli, V.; Aprea, P.; Scaldaferri, R.; Caputo, D. Optimization of the production process of BZT−BCT sol−gel thin films obtained from a highly stable and green precursor solution. *Materials and Manufacturing Processes* **2021**, *36* (14), 1642−1649.
(22) Xu, J.; Zhou, Y.; Li, Z.; Lin, C.; Zheng, X.; Lin, T.; Wang, F. Microstructural, ferroelectric and photoluminescence properties of Er^{3+}-doped $Ba_{0.85}Ca_{0.15}Ti_{0.9}Zr_{0.1}O_3$ thin films. *Mater. Chem. Phys.* **2021**, *262*, No. 124320.
(23) Liu, S.; Zhang, Z.; Shan, Y.; Hong, Y.; Farooqui, F.; Lam, F. S.; Yang, Z. A flexible and lead-free BCZT thin film nanogenerator for biocompatible energy harvesting. *Mater. Chem. Front.* **2021**, *5* (12), 4682−4689.
(24) Reddy, S. R.; Kumar, A.; James, A. R.; Prasad, V. B.; Roy, S. K. Ferroelectric and nano-mechanical properties of the chemical solution deposited lead-free BCZT films. *Materials Science and Engineering* **2021**, *265*, No. 115037. B
(25) Sharma, H.; Maurya, K. K.; Shah, J.; Kotnala, R. K.; Negi, N. S. Enhanced dielectric and ferroelectric properties of chemical solution processed lead-free $Ba_{1-x}Ca_xZr_{0.1}Ti_{0.9}O_3$ thin films. *Ferroelectrics* **2021**, *582* (1), 80−97.
(26) Wang, H.; Xu, J.; Ma, C.; Xu, F.; Wang, L.; Bian, L.; Chang, A. Spectroscopic ellipsometry study of $0.5BaZr_{0.2}Ti_{0.8}O_3 - 0.5Ba_{0.7}Ca_{0.3}TiO_3$ ferroelectric thin films. *Journal of alloys and compounds* **2014**, *615*, 526−530.
(27) Mandeljc, M.; Kosec, M.; Malič, B.; Samardzija, Z. Low temperature processing of lanthanum doped PZT thin films. *Integr. Ferroelectr.* **2000**, *30* (1−4), 149−156.
(28) Hoffmann, S.; Waser, R. Control of the morphology of CSD-prepared $(Ba,Sr)TiO_3$ thin films. *Journal of the European Ceramic Society* **1999**, *19* (6−7), 1339−1343.
(29) Mansour, C.; Benwadih, M.; Revenant, C. Sol−gel derived barium strontium titanate thin films using a highly diluted precursor solution. *AIP Advances* **2021**, *11* (8), No. 085302.
(30) Aygün, S. M.; Ihlefeld, J. F.; Borland, W. J.; Maria, J. P. Permittivity scaling in $Ba_{1-x}Sr_xTiO_3$ thin films and ceramics. *J. Appl. Phys.* **2011**, *109* (3), No. 034108.
(31) Pečnik, T.; Benčan, A.; Glinšek, S.; Malič, B. Tailoring the microstructure and dielectric properties of $Ba_{0.5}Sr_{0.5}TiO_3$ thin films by solution-based processing in the frame of the Microstructural Zone Model. *J. Alloys Compd.* **2018**, *743*, 812−818.
(32) Ihlefeld, J. F.; Maria, J. P.; Borland, W. Dielectric and microstructural properties of barium titanate zirconate thin films on copper substrates. *Journal of materials research* **2005**, *20* (10), 2838−2844.
(33) Teranishi, T.; Kajiyama, S.; Hayashi, H.; Kishimoto, A. Polarization behavior of sol-gel-derived relaxor $Ba(Zr,Ti)O_3$ films. *J. Am. Ceram. Soc.* **2017**, *100* (4), 1542−1550.
(34) Zhai, J.; Yao, X.; Shen, J.; Zhang, L.; Chen, H. Structural and dielectric properties of $Ba(Zr_xTi_{1-x})O_3$ thin films prepared by the sol−gel process. *J. Phys. D: Appl. Phys.* **2004**, *37* (5), 748.
(35) Singh, B.; Kumar, S.; Arya, G. S.; Negi, N. S. Room temperature structural and electrical properties of barium calcium titanate (BCT) thin films. *AIP Conf. Proc.* **2015**, *1661* (1), No. 060005, DOI: 10.1063/1.4915375.
(36) Jia, Q.; Shen, B.; Hao, X.; Song, S.; Zhai, J. Anomalous dielectric properties of $Ba_{1-x}Ca_xTiO_3$ thin films near the solubility limit. *Mater. Lett.* **2009**, *63* (3−4), 464−466.
(37) Konsago, S. W.; Žiberna, K.; Kmet, B.; Benčan, A.; Uršič, H.; Malič, B. Chemical Solution Deposition of Barium Titanate Thin Films with Ethylene Glycol as Solvent for Barium Acetate. *Molecules* **2022**, *27* (12), 3753.
(38) Livage, C.; Safari, A.; Klein, L. C. Glycol-based sol-gel process for the fabrication of ferroelectric PZT thin films: Code: EP28. *J. Sol-Gel Sci. Technol.* **1994**, *2*, 605−609.
(39) Uršič, H.; Prah, U. Investigations of ferroelectric polycrystalline bulks and thick films using piezoresponse force microscopy. *Proceedings of the Royal Society A* **2019**, *475* (2223), No. 20180782.
(40) Jung, W. S.; Min, B. K.; Park, J.; Yoon, D. H. Formation mechanism of barium titanate by thermal decomposition of barium titanyl oxalate. *Ceram. Int.* **2011**, *37* (2), 669−672.
(41) Barbatoa, P. S.; Casuscellib, V.; Apreaa, P.; Scaldaferrib, R.; Pedacib, I.; Caputoa, D. Green production of lead-free BZT-BCT thin films for applications in MEMS devices. *Chem. Eng. Trans.* **2021**, *84*, 97−102.
(42) Hoffmann, S.; Hasenkox, U.; Waser, R.; Jia, C. L.; Urban, K. Chemical Solution Deposited $BaTi0_3$ AND $SrTi0_3$ Thin Films with Columnar Microstructure. *MRS Online Proceedings Library (OPL)* **1997**, *474*, 9.
(43) Abazari, M.; Akdoğan, E. K.; Safari, A. Effect of manganese doping on remnant polarization and leakage current in $(K_{0.44},Na_{0.52},Li_{0.04})(Nb_{0.84},Ta_{0.10},Sb_{0.06})$ O_3 epitaxial thin films on $SrTiO_3$. *Appl. Phys. Lett.* **2008**, *92* (21), 212903.
(44) Birkholz, M.; *Thin film analysis by X-ray scattering*; John Wiley & Sons, 2006.
(45) Schenk, T.; Bencan, A.; Drazic, G.; Condurache, O.; Valle, N.; Adib, B. E.; Glinsek, S. Enhancement of ferroelectricity and orientation in solution-derived hafnia thin films through heterogeneous grain nucleation. *Appl. Phys. Lett.* **2021**, *118* (16), No. 162902.
(46) Konsago, S. W.; Debevec, A.; Cilenšek, J.; Kmet, B.; Malič, B. Linear Thermal Expansion of $0.5Ba(Zr_{0.2}Ti_{0.8})O_3$-$0.5(Ba_{0.7}Ca_{0.3})TiO_3$ Bulk Ceramic. *Inform. MIDEM* **2023**, *53* (4), 233−238.
(47) Okaji, M. Absolute thermal expansion measurements of single-crystal silicon in the range 300−1300 K with an interferometric dilatometer. *Int. J. Thermophys.* **1988**, *9*, 1101−1109.
(48) Jia, C. L.; Urban, K.; Hoffmann, S.; Waser, R. Microstructure of columnar-grained $SrTiO_3$ and $BaTiO_3$ thin films prepared by chemical solution deposition. *J. Mater. Res.* **1998**, *13* (8), 2206−2217.
(49) Ophus, C. Four-Dimensional Scanning Transmission Electron Microscopy (4D-STEM): From Scanning Nanodiffraction to Ptychography and Beyond. *Microsc. Microanal.* **2019**, *25*, 563−582.
(50) Amorín, H.; Venet, M.; García, J. E.; Ochoa, D. A.; Ramos, P.; López-Sánchez, J.; Algueró, M. Insights into the Early Size Effects of

Lead-Free Piezoelectric $Ba_{0.85}Ca_{0.15}Zr_{0.1}Ti_{0.9}O_3$. *Adv. Electronic Mater.* **2023**, *10*, No. 2300556.
(51) Noguchi, Y.; Miyayama, M. Effect of Mn doping on the leakage current and polarization properties in $K_{0.14}Na_{0.86}NbO_3$ ferroelectric single crystals. *Journal of the Ceramic Society of Japan* **2010**, *118* (1380), 711−716.
(52) Mgbemere, H. E.; Hinterstein, M.; Schneider, G. A. Structural phase transitions and electrical properties of $(K_xNa_{1-x})NbO_3$-based ceramics modified with Mn. *Journal of the European Ceramic Society* **2012**, *32* (16), 4341−4352.
(53) Borderon, C.; Nadaud, K.; Coulibaly, M.; Renoud, R.; Gundel, H. Mn-Doped $Ba_{0.8}Sr_{0.2}TiO_3$ Thin Films for Energy Storage Capacitors. *Int. J. Adv. Res. Phys. Sci.* **2019**, *6* (2), 2349−7882.
(54) Semenov, A.; Dedyk, A.; Mylnikov, I.; Pakhomov, O.; Eskov, A.; Anokhin, A.; Kholkin, A. Mn-doped $BaTiO_3$ ceramics: Thermal and electrical properties for multicaloric applications. *Materials* **2019**, *12* (21), 3592.
(55) Chi, Q. G.; Zhang, C. H.; Sun, J.; Yang, F. Y.; Wang, X.; Lei, Q. Q. Interface optimization and electrical properties of 0.5 $Ba(Zr_{0.2}Ti_{0.8})O_3$−0.5$(Ba_{0.7}Ca_{0.3})TiO_3$ thin films prepared by a sol−gel process. *J. Phys. Chem. C* **2014**, *118* (28), 15220−15225.
(56) Lin, Y.; Wu, G.; Qin, N.; Bao, D. Structure, dielectric, ferroelectric, and optical properties of $(1-x)Ba(Zr_{0.2}Ti_{0.8})O_3-x(Ba_{0.7}Ca_{0.3})TiO_3$ thin films prepared by sol−gel method. *Thin Solid Films* **2012**, *520* (7), 2800−2804.
(57) Chi, Q. G.; Zhu, H. F.; Xu, J. C.; Wang, X.; Lin, J. Q.; Sun, Z.; Lei, Q. Q. Microstructures and electrical properties of $0.5(Ba_{0.7}Ca_{0.3})TiO_3$−$0.5Ba(Zr_{0.2}Ti_{0.8})O_3$ thin films prepared by a sol−gel route. *Ceram. Int.* **2013**, *39* (7), 8195−8198.
(58) Nguyen, M. D.; Rijnders, G. Comparative study of piezoelectric response and energy-storage performance in normal ferroelectric, antiferroelectric and relaxor-ferroelectric thin films. *Thin solid films* **2020**, *697*, No. 137843.
(59) Silva, J. P.; Silva, J. M.; Oliveira, M. J.; Weingärtner, T.; Sekhar, K. C.; Pereira, M.; Gomes, M. J. High-performance ferroelectric−dielectric multilayered thin films for energy storage capacitors. *Adv. Funct. Mater.* **2019**, *29* (6), No. 1807196.
(60) Sivaramakrishnan, S.; Mardilovich, P.; Schmitz-Kempen, T.; Tiedke, S. Concurrent wafer-level measurement of longitudinal and transverse effective piezoelectric coefficients ($d_{33,f}$ and $e_{31,f}$) by double beam laser interferometry. *J. Appl. Phys.* **2018**, *123* (1), No. 014103, DOI: 10.1063/1.5019568.
(61) Matavž, A.; Bradeško, A.; Rojac, T.; Malič, B.; Bobnar, V. Self-assembled porous ferroelectric thin films with a greatly enhanced piezoelectric response. *Applied Materials Today* **2019**, *16*, 83−89.

https://doi.org/10.1021/acsaelm.4c00530
ACS Appl. Electron. Mater. 2024, 6, 4467−4477